Exploiting low-grade waste heat to produce electricity through supercapacitor containing carbon electrodes and ionic liquid electrolytes

Electrochimica Acta 403 (2022) 139640

Contents lists available at ScienceDirect

Electrochimica Acta

journal homepage: www.elsevier.com/locate/electacta

Exploiting low-grade waste heat to produce electricity through supercapacitor containing carbon electrodes and ionic liquid electrolytes

Mazharul Haque[a,*], Iqbaal Abdurrokhman[b], Alexander Idström[b], Qi Li[c], Azega Rajaras[a,d], Anna Martinelli[b], Lars Evenäs[b,d], Per Lundgren[a], Peter Enoksson[a,d,e]

[a] Micro and Nanosystems Group, Department of Microtechnology and Nanoscience, Chalmers University of Technology, Gothenburg, Sweden
[b] Department of Chemistry and Chemical Engineering, Chalmers University of Technology, Gothenburg, Sweden
[c] Chalmers University of Technology, Gothenburg, Sweden
[d] Wallenberg Wood Science Center, Chalmers University of Technology, Gothenburg, Sweden
[e] Enoaviatech AB, Stockholm, Sweden

ARTICLE INFO

Article history:
Received 23 July 2021
Revised 1 October 2021
Accepted 21 November 2021
Available online 1 December 2021

Keywords:
Low-grade heat
Thermal charge
Supercapacitor
Ionic liquid
Self-diffusion coefficient
Temperature gradient

ABSTRACT

Low-grade thermal energy harvesting presents great challenges to traditional thermoelectric systems based on the Seebeck effect, the thermogalvanic effect, and the Soret effect due to fixed temperature gradient and low voltage output. In this study, we report an ionic thermoelectric system, essentially a supercapacitor (SC) containing an ionic liquid (IL) electrolyte and activated carbon electrodes, which works on the thermocapacitive effect and does not require any fixed temperature gradient, rather it works in a homogeneously changing temperature. A systematic investigation is carried out on SCs containing two different ILs, 1-Ethyl-3-methylimidazolium bis (trifluoromethylsulfonyl), EMIm TFSI, and 1-Ethyl-3-methylimidazolium acetate, EMIm OAc. A high voltage output of 176 mV is achieved for EMIm TFSI containing SC by exposing just to 60 °C environment. Moreover, a large voltage of 502 mV is recovered from the SC upon subjecting to heat after one electrical charge/discharge cycle. A system containing two SCs in series demonstrates a significant voltage of 947 mV. The observed performance difference between the two ILs is rationalized in terms of the extent of asymmetry in the interfaces of the electrical double layer that essentially originates from different diffusivity of individual ions. The mechanism can be applied to a plethora of ILs to exploit low-grade heat to store electricity without a fixed temperature gradient, opening up the possibility to merge different scientific communities and enrich this rising research field.

1. Introduction

Thermal energy is an omnipresent energy resource that is generated as a byproduct of various industrial processes as well as non-industrial sources such as power plants and heat pumps. The majority of this energy is unused and stays in the surroundings as waste heat; in fact, 63% of the waste heat emerges or is readily available at a temperature below 100 °C [1]. Generally, the heat in this temperature range is defined as low-grade thermal energy. Recovery of this waste heat holds enormous prospects, not just limited to improving energy and fuel efficiency of related processes, but also extended to capturing energy from abundant resources like solar-, geo-, and ocean thermal energy.

There are commonly three methods to convert heat into electricity: (I) Mechanical heat engines [2], where the thermal energy transforms into mechanical work that is successively utilized to drive an electric generator. This method is impractical to apply to a distributed heat source; (II) Thermoelectric engines or thermoelectric generators that convert heat directly into electrical current [3] based on the Seebeck effect; (III) Ionic thermoelectric systems, which are based on either thermogalvanic and/or ionic thermodiffusion effect – also known as the Soret effect [4]. The thermoionic systems are receiving increased attention owing to their capability of producing a large voltage output from a small temperature gradient [5] compared to other technologies and devices (thermoelectrics).

When a cell containing redox-electrolyte is retained in a fixed temperature gradient, a thermovoltage arises, proportional to the reaction entropies of the redox couples in the electrolyte near the

* Corresponding author.
E-mail address: mhaque@chalmers.se (M. Haque).

https://doi.org/10.1016/j.electacta.2021.139640

Table 1
Working mechanism and performance metric of the different thermoelectric systems.

Thermoelectric systems	Device	Underlying physics	Mechanism	Operation mode
Solid-state thermoelectric generator	Thermoelectrics	Seebeck effect	Diffusion of electrons or holes	Continuous
Ionic-thermoelectric system	Thermocell	Thermogalvanic effect	Temperature-dependent redox reaction	Continuous
Ionic-thermoelectric system	Thermoionic capacitor	Soret /thermocapacitive effect	Diffusion of ions	Intermittent

hot and the cold side. This phenomenon is known as thermogalvanic effect, and the device is called thermocell. On the other hand, the ionic thermodiffusion effect does not involve any redox activity, but rather relies on the net amount of entropy carried by thermodiffusive ions driven by the temperature gradient. If the thermal mobility of cations and anions are different, a local net ionic charge carrier concentration develops, resulting in an electrical field. The corresponding device is a thermoionic capacitor. In an electrochemical cell, this electrical field creates a potential difference between the hot and cold electrodes of the cell [4,6]. Table 1 compares the mechanisms and operation mode of various thermoelectric systems [7].

Producing a fixed temperature gradient between two electrodes in an electrochemical cell is the most typical approach to create different thermal responses in the two interfaces of an ionic thermoelectric system, however, presenting drawbacks in extra energy consumption and high device volume. In essence, to maintain the fixed temperature gradient the two electrodes are kept quite far from each other, which increases the internal resistance of the system and adversely affects the power performance [8]. Shortening the distance between the electrodes could improve the performance, but it would require additional energy to maintain the temperature gradient. Alternatively, if the two interfaces hold inherently dissimilar characteristics, it is possible to create a difference in the thermal response without a fixed temperature gradient, relying instead on a uniform change in temperature [8,9]. Thermal charging without the need to maintain a fixed temperature gradient is significantly advantageous from a design perspective since it is very difficult to maintain a fixed temperature gradient at a low-grade waste heat regime [7]. If maintaining the temperature gradient is not the concern, then the distance between the electrodes could also be minimized. Consequently, the structure of the device would be the same as a supercapacitor (SC) consisting of porous carbon electrodes and ionic electrolytes [10].

Theoretically, even though the thermogalvanic effect can also contribute to thermal energy conversion due to the surface functional groups, the thermoionic effect is most predominant in carbon-based SC upon temperature change. When an electrolyte is confined within a porous electrode, both the cations and anions are under the influence of different force fields, and they exhibit an anisotropic structure that leads to a net interface potential without any external electrical bias [11,12]. The ionic structures and behavior in the interfacial double layer are strongly influenced by temperature [13,14], and an increased output voltage can be achieved with increasing temperature. Besides, non-uniform pore distributions in high surface area carbon materials, which often include branched pores with different diameters, result in different relaxation processes over the surface. Therefore, a significant portion of the charge stays unused in a typical electrical charge/discharge cycle due to the difference in kinetics between the fast movement of free electrons and the slower movement of counterions at the interface. At the end of discharge, this unused charge slowly increases the open-circuit voltage [15]. When the device is subjected to a high-temperature environment, the unused charge can be harvested faster by increasing the movement of counterions and the extent of voltage rise will be significantly higher. To sum up, SCs containing porous carbon electrodes and ionic liquid (IL) electrolytes with different properties of cations and anions have a great potential of utilizing low-grade waste heat to store electrical energy in a homogeneously varying temperature. ILs are particularly suitable for this type of device due to their high thermal and electrochemical stability, high ion density, and very low flammability [16,17]. Essentially, they are organic salt solely composed of bulky, asymmetric organic cations and weakly coordinating small inorganic or organic anions. Due to this unique combination of large cation and charge-delocalized anions, they stay liquid at temperatures below 100 °C [18]. By combining different ratios of cations and anions [19] the physical and chemical properties of ILs can be tuned virtually in an unlimited way, which is an attractive feature for an electrolyte. Among different ILS, imidazolium-based ILs have exhibited an outstanding electrochemical performance due to their relatively high ionic conductivity and low viscosity [20,21]. Owing to these unique features ILs are also utilized in polymer electrolytes to overcome their intrinsic low conductivity in a wide range of temperatures where ILs act as plasticizer [22,23]. Most importantly, as they are solvent-free unlike organic or aqueous electrolytes, they are perfect candidates to study the ionic interactions that result in asymmetry in the electrical double layers, which is necessarily responsible for dissimilar interfacial properties that facilitate voltage output in an ionic thermoelectric system.

In this study, we investigated SCs consist of activated carbon electrodes and two different IL electrolytes, namely: 1-Ethyl-3-methylimidazolium bis (trifluoromethylsulfonyl) imide, EMIm TFSI, and 1-Ethyl-3-methylimidazolium acetate, EMIm OAc from room temperature to 60 °C. The study reveals that due to a substantial difference in the self-diffusion coefficient of $[EMIm]^+$ in EMIm TFSI compared to $[EMIm]^+$ in EMIm OAc, a larger voltage output can be achieved with the device containing EMIm TFSI electrolyte compared to the device containing EMIm OAc electrolyte. When the devices are subjected to heat at the end of the electrical charge/discharge cycle, a significant increase of voltage rise can be observed, which opens the possibility to assign a parallel life to SCs.

2. Experimental

2.1. Materials and assembly of coin cell devices

Activated carbon electrodes were prepared using a high surface area activated carbon powder (Kuraray®, YP-80F), conductive agent carbon black, and polytetrafluoroethylene (PTFE) binder (60 wt. % in H_2O) in a weight ratio of 80:10:10. The as-prepared electrode materials contain an even distribution of micropores and mesopores with a surface area of 1565 ± 30 $m^2\ g^{-1}$. The elemental analysis demonstrates that the activated carbon powder contains 94.1 at.% carbon along with 5.90 at.% oxygen with some acidic surface oxygen functional groups such as phenol and ethers, carbonyl, carboxyl, and lactones. The detailed electrode preparation and material characterization regarding surface morphology, surface area, and elemental composition can be found in our previous article [21]. The individual electrode pellet was approximately 3.18 mg cm^{-2} in mass loading (2.5 mg in mass with a geometrical area of 0.785 cm^2), and 100 µm in thickness.

A commercially available glass fiber sheet (GF, Whatman®) with 200 µm thickness and a diameter of 16 mm was used as the separator.

1-Ethyl-3-methylimidazolium bis (trifluoromethylsulfonyl) imide 97% (EMIm TFSI, Sigma Aldrich) and 1-Ethyl-3-methylimidazolium acetate 97% (EMIm OAc), Sigma Aldrich) were used as electrolyte solutions without any further purification.

Symmetric two-electrode devices were prepared with the above-mentioned materials in a CR2025 coin cells consisting of a SS304 stainless steel casing, an O-ring sealant, a stainless steel spring spacer, and a stainless steel current collector. Two devices were prepared without any activated carbon, but rather stainless steels were used as active electrodes in combination with both the ILs. Electrochemical measurements were carried out 24 h after cell assembly, in order to provide enough time for electrolyte adsorption. Approximately 100 µL of electrolyte was injected into each device.

2.2. Conductivity measurements of ionic liquid

The conductivity measurement was carried out using a Broadband Dielectric spectrometer from Novocontrol GmbH at different temperatures, 25, 35, 45, and 60 °C. The ILs were placed in a cell containing two stainless steel electrodes with a diameter of 5 mm. The thickness of the samples was controlled to be 3.1 mm using a PTFE spacer. The measurements covered a wide frequency range from 10^{-1} to 10^{7} Hz. The temperature was controlled using a nitrogen gas cryostat with stability of ±0.5 °C and the samples were equilibrated for 600 s at each temperature.

2.3. Viscosity and density measurements of ionic liquid

The viscosity measurements were conducted in TA instrument Rheometer DHR3 model equipped with a Peltier heating plate in the same temperature range as the conductivity measurements. Cone and plate geometry with a $\phi = 40$ mm, angle of 1°, and a truncation gap of 26 µm were selected for the experiments. All the measurements were conducted in an open-air environment.

2.4. Pulsed-field gradient NMR spectroscopy

The self-diffusion coefficients for the ILs at different temperatures were studied using an AVANCE III HD Bruker NMR spectrometer, operating at 14.1 T, equipped with a diff30 probe. The diffusion coefficients were analyzed at 298.0, 308.0, 318.0, and 333.0 K. Each temperature was calibrated using pure methanol or pure ethylene glycol prior to the experiments.

Self-diffusion coefficients for both anion and cation of the two ILs were obtained using ^{1}H and ^{19}F 5 mm coil insets, respectively. The specific parameters were individually set for each sample. For the ^{1}H experiments, a 16 µs ^{1}H-pulse, 0.4 s acquisition time, 5–12 s recycle delay, and 40 kHz spectral width, were used. For the ^{19}F experiments, a 14 µs ^{19}F 90 degree-pulse, 2 s acquisition time, 2 s recycle delay, and 7 kHz spectral width were used. The chemical shifts were calibrated using tetramethylsilane as an external reference.

For the diffusion experiments, a double stimulated echo (diffDste) was used in order to handle the convection in the ILs at high temperatures. The measurements were conducted using 16 scans at 16 gradient steps. The parameters for both ^{1}H and ^{19}F were optimized to obtain full attenuation of the signal, including Δ=100 ms, δ = 1–2 ms, and linear increments of g to g_{max} of 200–600 G/cm. Correct calibration of the gradient amplifier was verified by obtaining the self-diffusion coefficient of HDO trace in a standard sample of pure D_2O [24]. The self-diffusion coefficients (D) of the individual ions were estimated by fitting the Stejskal-Tanner equation [25] to the signal integral intensity attenuation data according to

$$I = I_0 \exp\left\{-D(\gamma g \delta)^2(\Delta - \delta/3)\right\} \quad (1)$$

where I is the signal intensity, I_0 the signal intensity at zero gradient, Δ the diffusion delay, δ the gradient pulse duration, γ the gyromagnetic ratio of the nucleus studied, and g the gradient strength. Least-squares fitting of parameters I_0 and D with nonlinear dependence using the Levenberg–Marquardt method was applied [26].

2.5. Measurement protocol

2.5.1. Thermovoltage measurement

Open circuit voltage (OCV), or voltage output, was monitored in two periods: the first period is to observe the voltage rise, and the second period is to observe the change of achieved voltage. Afterward, the devices were electrically discharged to 0 V at RT with a constant current. Four different conditions were applied to observe the extent of voltage output. In the first condition, the devices are shorted for 15 mins to ensure that they are fully discharged to 0 V, then exposed to 60 °C followed by bringing them back to RT. The second condition involves one electrical charge/discharge cycle at RT, prior to high-temperature exposure. The third and fourth conditions are analogous to the previous two, but instead of exposing the devices to the high-temperature environment, they were kept at RT throughout the measurement period in order to identify the influence of heat on the observed voltage output.

After the initial scrutiny, two devices containing EMIm TFSI and AC electrodes were connected in series, and voltage rise was recorded upon applying the second condition mentioned above. OCV was monitored for a period of 5300 s during high-temperature exposure followed by 3600 s while returning to RT.

The devices were subjected to heat by placing them in a DZF-6020 oven (temperature fluctuation ±1 °C). The temperature was further monitored by a UT61B Modern Digital Multimeter coupled with a thermal sensor connected to the devices. The sensor accuracy is ±1.2 % in a temperature range of -40 to 1000 °C.

2.5.2. Electrochemical measurement

Electrochemical characterizations of the devices were carried out by cyclic voltammetry (CV), Galvanostatic charge/discharge (GCD), and electrochemical impedance spectroscopy (EIS) at both RT and 60 °C. Additionally, single frequency EIS was conducted to the device containing AC electrodes with a fixed frequency of 500 mHz for 3 h in the high-temperature environment, in order to monitor the change of the impedance of the devices.

All electrochemical measurements were conducted using a Gamry Reference 3000AE Galvanostat/Potentiostat workstation with a current accuracy (±10 pA ±0.3 %) and voltage accuracy of (±1 mV ±0.3 %) of reading.

The values of capacitance were calculated from both CV and GCD plots according to:

$$C_{s,CV} = 4 \times 1000 \times \frac{\int_0^{2\cdot\Delta V/\upsilon_s} |i| dt}{2 \cdot m \cdot \Delta V} \quad \left(\mathrm{F\,g^{-1}}\right) \quad (2)$$

$$C_{s,GCD} = 4 \times \frac{I_d \cdot t_d}{m \cdot V_d} \quad \left(\mathrm{F\,g^{-1}}\right) \quad (3)$$

where $C_{s,CV}$ is the specific capacitance from a CV plot, i (A) is the current response as a function of time t (s), ΔV is the working voltage range, υ_s (mV s^{-1}) is the scan rate, $C_{s,GCD}$ is the specific capacitance from a GCD plot, I_d is the discharge current, t_d is the discharge time, V_d is the voltage range excluding internal resistance (IR) drop, and m is the total mass of both electrodes (each electrode had approximately the same mass). The factor of 4 modifies

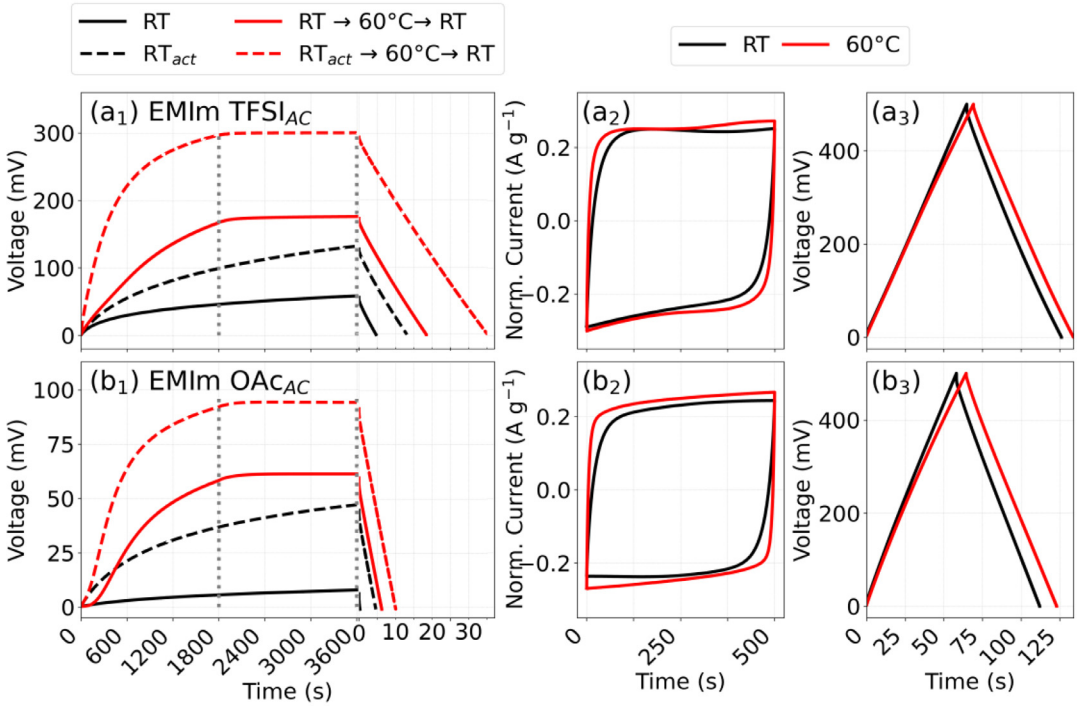

Fig. 1. Thermal and electrical characterization of devices containing AC electrodes and IL electrolytes: voltage output (a_1) EMIm TFSI, (b_1) EMIm OAc with different conditioning, CV (a_2) EMIm TFSI, (b_2) EMIm OAc with a scan rate of 20 mV s^{-1}, GCD (a_3) EMIm TFSI, (b_3) EMIm OAc with a constant current of 10 mA g^{-1}.

the device capacitance (normalized to the mass of two electrodes) to the capacitance of a single electrode.

Power density and energy density of the devices were calculated from GCD measurements according to:

$$C_d = \frac{C_{s,GCD}}{4} \quad \left(\mathrm{F\,g^{-1}}\right) \tag{4}$$

$$E = \frac{1}{2} \times \frac{C_d \cdot {V_d}^2}{3.6} \quad \left(\mathrm{Wh\,kg^{-1}}\right) \tag{5}$$

$$P_{\mathrm{avg}} = 3600 \times \frac{E}{t_d} \quad \left(\mathrm{W\,kg^{-1}}\right) \tag{6}$$

where C_d is the specific device capacitance from GCD measurements, E is the energy density and, P_{avg} is the average power density of the device. The numbers 3.6 and 3600 are unit conversion factors.

3. Results and discussions

3.1. Thermal and electrical capacitive properties of porous AC electrode containing devices

Fig. 1 demonstrates the thermal and electrical capacitive properties of both devices containing EMIm TFSI and EMIm OAc IL electrolytes. Systematic conditioning is applied to the devices in order to understand the thermal charging behavior such as (i) spontaneous voltage rise at RT, (ii) voltage rise after one electrical charge/discharge cycle at RT (termed RT$_{act}$-cycle), (iii) voltage rise at the high-temperature environment, and (iv) voltage rise at high-temperature environment after one RT$_{act}$-cycle, see Fig. 1 (a_1) and (b_1).

A spontaneous voltage rise until 3600 s can be noticed for both the devices at RT, 59 and 8 mV for EMIm TFSI and EMIm OAc, respectively. When the devices have gone through one electrical charge/discharge cycle, RT$_{act}$-cycle, an increased voltage rise of 132 mV (EMIm TFSI) and 47 mV (EMIm OAc) can be noticed. Voltage rise further increases when the devices are exposed to heat, 176 mV (EMIm TFSI) and 61 mV (EMIm OAc). A maximum voltage output is achieved when the devices are exposed to heat after the RT$_{act}$-cycle, 300 mV and 94 mV for EMIm TFSI and EMIm OAc, respectively.

When a porous electrode is incorporated into the system, ILs wet the micropores, and spontaneous adsorption of ions takes place without any external bias [27]. Depending on the nature of cations, anions, and their interaction with each other, different adsorption rates occur in the positive and negative electrodes, creating a potential difference between the two interfaces. Therefore, the observed voltage rise at RT for both the devices is quite reasonable, noticed in several other studies [15,28] as well. When heat is applied to a system containing an IL, valid to any electrolyte solution, several thermal modifications can occur such as a change in the volume (due to solvent expansion), chemical potential, viscosity, ionic conductivity, etc. [7]. Apart from these modifications, one very important phenomenon occurs which is the development of concentration gradients of the ions due to local non-homogeneity in the electrolyte solution. Depending on the relative motion between cations and anions, governed by their migration properties, ion density increases quite significantly near the interfaces and amplifies the adsorption rate. Consequently, the electrochemical potential of the interfaces increases and exhibits increased voltage output compared to the voltage output from the spontaneous interfacial potential at RT, which is quite clear in Fig. 1 (a_1) and (b_1).

When the devices go through one RT$_{act}$-cycle and are exposed to heat, the observed voltage output is significantly higher than the previous two conditions, although the origin of such a high voltage still lies in the interfacial properties. An effective representation of the interface containing porous electrode was realized in terms of a RC transmission line model, originally proposed by de Levie [29]. According to the model, the interface can be thought of as an equivalent circuit consisting of different resistors (R) and capacitors (C) associated with the diverse branches of the pores con-

taining different (RC) time constants. A mathematical evaluation of the model showed that the potential and current distribution throughout the porous electrode do not proceed evenly, mostly due to IR drop in the electrolyte solution within the pores. Consequently, faster charge storage or release occurs at the mouth of the pores compared to the base of the pores, leaving a gradient of potential distributed along the pore walls that does not participate during the RT_{act}-cycle and stays "*unused*". Therefore, even though by definition at the end of discharge the devices should hold zero voltage, they exhibit a voltage rise, known as the "*voltage rebound effect*" [15]. This voltage rebound effect largely originates from the movement of the charge carriers from the base of the pores that were "*unused*" during the initial RT_{act}-cycle to the tip of the pores in the open-circuit configuration [28]. The extent of voltage rise when the devices are exposed to heat after the RT_{act}-cycle is significantly higher (almost three times) compared to the voltage rise at RT after the RT_{act}-cycle. As the increase of ionic conductivity in high temperature is significant compared to the decrease of electrical conductivity of carbon electrodes, electrolyte ions play a dominant role in the observed voltage rise.

It can also be noticed that the voltage increase for the heat-exposed devices is quick in the beginning (over the first 1800 s) and then reaches a saturation (at the end of 1800 s) due to equilibrium of thermal diffusion and mass diffusion in the system. The equilibrium condition retains even if the devices are removed from the high-temperature environment (after 1800 s) because at this point the ions are held electrostatically in the interface. On the other hand, OCV keeps on rising for the devices at RT albeit at a slower rate, indicating that the voltage output is going to be significantly smaller compared to the heat-exposed devices, and a considerably longer time will be needed to reach an equilibrium. This further illustrates the influence of heat to recover a faster and larger voltage output. Owing to the high thermal stability of ILs, temperature exposure is not just limited to 60 °C but could easily be extended to over 100 °C. Generally, with temperature increase, the dielectric properties of liquid electrolytes reduce due to increased thermal motion of the electrolyte ions. Therefore, the real capacitance decreases with increasing temperature. However, at the same time with increasing temperature, the resistance decreases as well. Consequently, more equivalent capacitance is gained (due to lowered resistance/increased ionic conductivity) than is lost by thermal agitation of electrolyte ions [30]. Because of this advantageous trade-off, improved capacitive performance at a temperature over 120 °C is observed in a previous study containing EMIM OAc electrolyte [21]. Unfortunately, in the current study, the temperature exposure is only limited to 60 °C due to the thermal instability of the encapsulated coin cell components, particularly the plastic gasket rings that maintain the separation between the two electrodes. However, if the devices are exposed at an even higher temperature, for instance at 100 °C, the voltage output would be larger and faster. Thermodynamic force originating from the high temperature exposure drives the system out of equilibrium and hence initiates the thermodiffusion of ions. Eventually the system reaches to a steady state with a force-balanced interplay between the thermal diffusion and resultant electropotential gradient [4]. With increasing temperature, the extent of thermal diffusion, electropotential gradient will be larger and the steady-state will be reached faster as observed in both thermocell (thermogalvanic effect) [31] and thermoionic capacitor (capacitive effect) [32].

Generally, SCs suffer from self-discharge dictated by both electronic and ionic charge redistribution associated with the RC time constant in addition to the electrolyte ion diffusion [33]. However, as can be seen within the timeframe of these experiments, thermally charged devices do not suffer from self-discharge most likely due to a combination of relatively lower nominal voltage and reduced RC time constant [34]. To verify the extent of self-discharge for a longer period, an additional measurement has been carried out on the device containing EMIm TFSI as can be seen in Fig. S_1. After thermal charging for 4 h device was taken out from the high-temperature environment and self-discharge was monitored at RT for additional 4 h, where voltage decay was insignificant at the end of the measurement.

After temperature exposure, the devices are discharged electrically with a constant current of 10 mA g^{-1} at RT in order to study the capacitive performance, Fig. 1 (a_1) and (b_1). Capacitive performance is also investigated with typical electrochemical measurements such as CV (Fig. 1 (a_2) and (b_2)) and GCD (Fig. 1 (a_3) and (b_3)) on the same devices within a voltage window of 500 mV with a scan rate of 20 mV s^{-1} and 10 mA g^{-1}, respectively, at both RT and 60 °C. The linear charge/discharge curve from GCD, the rectangular shape of the CV, and the linear discharge curve of the thermally charged devices are typical signatures of capacitive behaviors [35]. The capacitance calculated from the GCD for EMIm TFSI containing devices at both RT and 60 °C is 50 and 52 F g^{-1}, which is very similar to the capacitance from the thermally charged device (EMIm TFSI, RT_{act}→60 °C→RT), 47 F g^{-1} (values from the other conditionings are comparable). The capacitance of EMIm OAc-containing devices at RT and 60 °C is 44 and 47 F g^{-1}, which is also very close to the capacitance value from the thermally charged device (EMIm OAc, RT_{act}→60 °C→RT), 43 F g^{-1} (values from the other conditionings are comparable). This demonstrates that thermally and electrically charged devices inherit a similar electrochemical signature.

The energy density is directly proportional to the square of the voltage, thus a high voltage output is desirable. In this regard, the voltage output for EMIm TFSI containing devices is significantly higher at each conditioning compared to the devices containing EMIm OAc. Both the devices have the same structure and components including electrodes and separator, therefore the observed difference originates either from the interactions among ions in the electrolytes or from the interaction of the electrolytes with the porous carbon electrodes. Generally, carbon materials have different surface functional groups attached to them, originating from the pristine source of the materials or different carbonization conditions [36]. Often, surface functional groups contribute to the charge storage by surface-confined redox reaction, which is temperature-dependent and may reflect the kinetics of the thermally induced charge storage [9] beside the ion confinement in the micropores. Therefore, in the next section, we investigate the performance of the devices with non-porous electrodes in order to verify the electrolyte contribution to the observed difference in the voltage output.

3.2. Thermal and electrical properties of electrolytes in non-porous electrode containing devices

Fig. 2 demonstrates the voltage rise of the devices containing flat stainless steel electrodes in combination with the two ILs, EMIm TFSI and EMIM OAc. The flat surface should exclude the ion confinement effect and contribution from the surface functional groups that generally occur in the porous electrodes. Similar conditioning as for the carbon electrode-containing devices is applied to these sets of measurements. As can be seen from Fig. 2 (a_1) and (b_1), the trend of the voltage rise with different conditioning is very similar to the previous measurements, although the voltage saturation occurs much earlier for the devices exposed to heat with the RT_{act}-cycle. When the devices are removed from the heat, the output voltage decreases to some extent as the ions try to reach a new equilibrium. Most likely, given enough time, the voltage will eventually reduce to a similar voltage as OCV at RT.

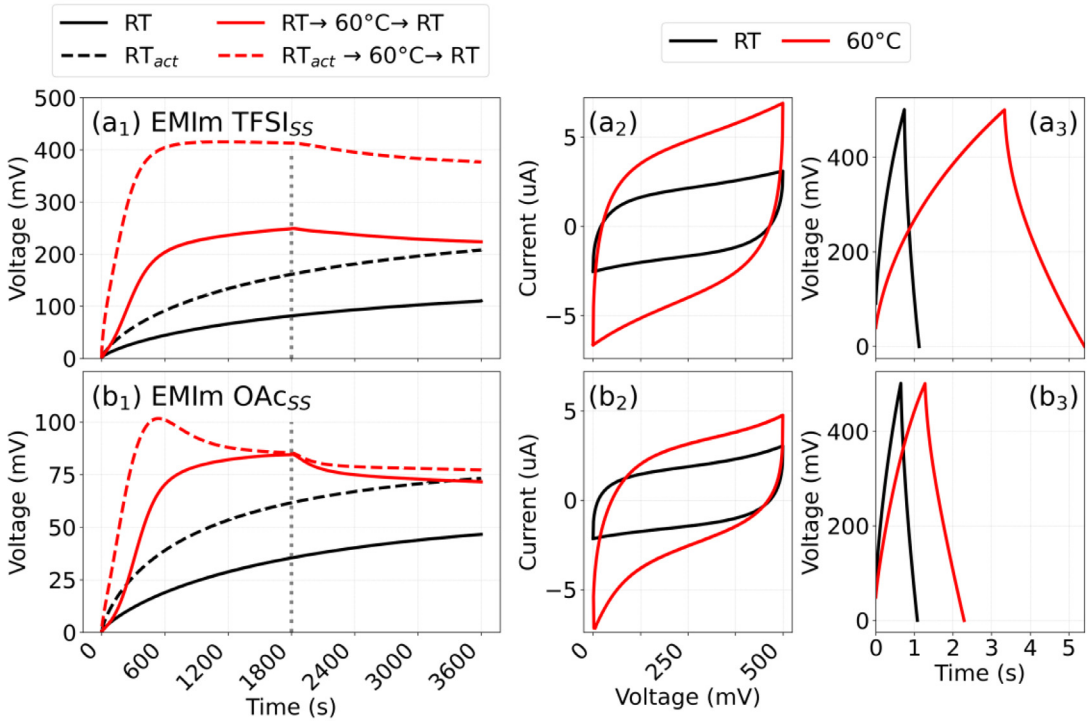

Fig. 2. Thermal and electrical characterization of devices containing SS electrodes and IL electrolytes: voltage output (a_1) EMIm TFSI, (b_1) EMIm OAc with different conditioning, CV (a_2) EMIm TFSI, (b_2) EMIm OAc with a scan rate of 20 mV s^{-1}, GCD (a_3) EMIm TFSI, (b_3) EMIm OAc with a constant current of 30 µA.

The fast voltage saturation is reasonable: as the surface area of the stainless steel electrode is significantly lower than the AC electrode, the electrochemical potential gradient will act on much earlier than the AC electrode-containing devices. During the heating period, the voltage stays relatively constant for the EMIm TFSI device once it reaches the maximum, whereas it starts dropping immediately for EMIm OAc-containing device. This gives a hint of how the transport properties of these two electrolytes may be differently influenced by temperature. However, when we compare the electrical performance, as can be seen from the CV Fig. 2 (a_2), (b_2), and GCD Fig. 2 (a_3), (b_3), the capacitive signature and performance of the devices are very similar at both RT and 60 °C. The stored charge with the stainless steel electrode is insignificant (due to very low surface area) compared to the AC electrode containing devices, but the observed higher output voltages for EMIm TFSI device compared to EMIm OAc device confirms that the achieved thermovoltage is independent of the electrodes and, needless to say, that interface with high surface area is still desirable.

3.3. EIS behavior of the devices containing AC electrodes, and dynamic properties of ILs

Fig. 3 (a_1) and (a_2) is a typical representation of the Nyquist plot at both RT and at 60 °C. EIS has been carried out in a wide frequency range of 10 mHz to 100 kHz with an (alternating current) ac perturbation of 10 mV. Unlike the CV and GCD technique, EIS is non-invasive and therefore can provide a detailed mapping of the electrolyte transport in the device. The first intersection point of the semicircle at the highest frequency region is essentially the equivalent series resistance (ESR), which primarily originates from the bulk electrolyte. The second intersection of the semicircle is interfacial resistance (R_{int}), related to the interface but still mostly dictated by the electrolyte. At this high-frequency range, the current response is completely in phase with the perturbation voltage and the system behaves in a purely resistive way because the electrolyte ions are not able to move through the EDL at such a high rate. In the mid-frequency region, the resistance of the interface exhibits a line with a 45° slope, which is associated with the charging of EDL. It is from this region that the charging of different RC elements of the porous network of the carbon electrodes can be realized. As sequential charging occurs from the pore mouth to the pore base, charging in this region is termed asynchronous charging [30]. At the point (frequency) where the 45° slope changes to 90°, asynchronous charging transforms to synchronous charging, and the system starts behaving in a capacitive way. Eventually, at the lowest frequency range, the current is ideally completely out of phase (-90°) with the perturbation voltage and the system behaves in a purely capacitive way. The transition frequency, where the 45° slope changes to 90°, is known as knee frequency and can give a qualitative measure of electrolyte diffusion to the porous electrodes [37].

As can be seen from Fig. 3 (a_1) and (a_2), the ESR and R_{int} values at RT are 0.95 and 2.31 Ω cm^2 for EMIm TFSI containing device, and 1.02 and 2.49 Ω cm^2 for EMIm OAc containing device. These values reduce at 60 °C for both the devices, specifically to 0.31 and 0.60 Ω cm^2 for EMIm TFSI and 0.33 and 0.70 Ω cm^2 for EMIm OAc. There is a difference in the values at RT, but the difference becomes marginal at 60 °C.

In general, the dynamics of ILs are largely dependent on the particular chemical structure of the ions that promote different interactions such as electrostatic, van der Waals interaction, hydrogen bonding, and π-π stacking. The cumulative effect from all these interactions leads to specific microstructures in the form of ionic aggregates, or clusters in nanodomains that define the overall ionic mobility. For instance, an increasing number of carbons in the alkyl chains and larger cation size induces a stronger van der Waals interaction, which limits the mobility of the charge carriers, thereafter frictional forces among ions, aggregates, and clusters result in an enhanced viscosity [38]. The size and shape of the anions also play a significant role, for instance, ILs containing large anions

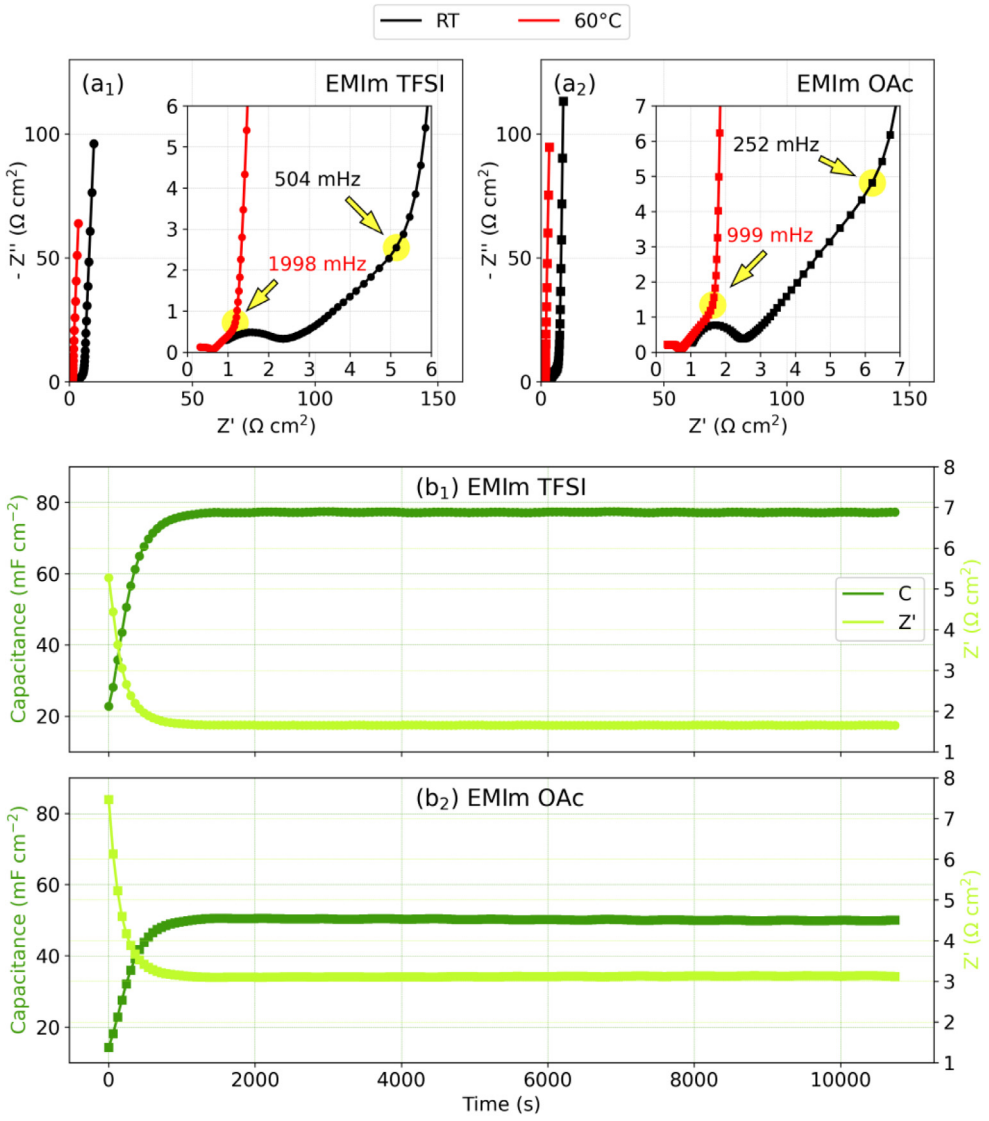

Fig. 3. EIS of both the devices at RT and 60 °C (a_1) EMIm TFSI, (a_2) EMIm OAc, Single frequency EIS at 500 mHZ (b_1) EMIm TFSI, (b_2) EMIM OAc during the heating from RT to 60 °C.

possess low charge density reducing the interactions among the ions and attribute to low viscosity. The symmetric shape of the anions provides an even charge distribution that forms more interaction with neighboring ions and hence increases the viscosity [39]. However, increasing temperature changes the rotational and translational energies of the ions and reduces the aggregation of molecules by improving ion mobility and reducing hydrogen bonding [40]. Therefore, viscosity decreases significantly with increasing temperature. Similarly, a decrease in resistance or increase in conductivity with temperature is also a known phenomenon, although absolute values can differ to some extent due to impurity or the measurement setup, the trend remains the same [38,41]. We have carried out the ionic conductivity and viscosity measurements of both EMIm TFSI and EMIm OAc ILs in the temperature range of 25–60 °C. The results are listed in Table 2.

It can be seen that viscosity decreases and ionic conductivity increases with temperature, and the difference between the two ILs becomes smaller at 60 °C. The trend of these values is consistent with the impedance behavior of the devices.

Since the ionic conductivity of the two electrolytes is similar at elevated temperatures, the significant difference between the voltage output of the two devices cannot be justified by the high-frequency impedance characteristics but must find explanations in the low-frequency region, starting from the knee frequency. It can be seen from Fig. 3 (a_1) and (a_2) that at RT the knee frequency for EMIm TFSI containing device is twice that of EMIm OAc containing device. At 60 °C, the knee frequency increases for both the devices, but the difference between the devices remains the same. The diffusion of the electrolyte ions is directly proportional to the knee frequency according to the equation [42,43], $D = \omega R^2$, where ω is the knee frequency, R is the characteristic distance ions travel (in this system, R is the thickness of the electrodes, which is similar for both the devices). From the equation, it is seen that the higher

Table 2
Viscosity and ionic conductivity of the studied ILs in a temperature range of 25 °C to 60 °C.

	Viscosity (mPa. s)		Ionic conductivity (mS cm^{-1})	
Temperature	EMIm TFSI	EMIm OAc	EMIm TFSI	EMIm OAc
25 °C	31.35	65.60	3.19	2.25
35 °C	22.50	34.00	4.21	3.06
45 °C	17.05	21.02	5.33	5.10
60 °C	11.95	13.45	8.07	7.94

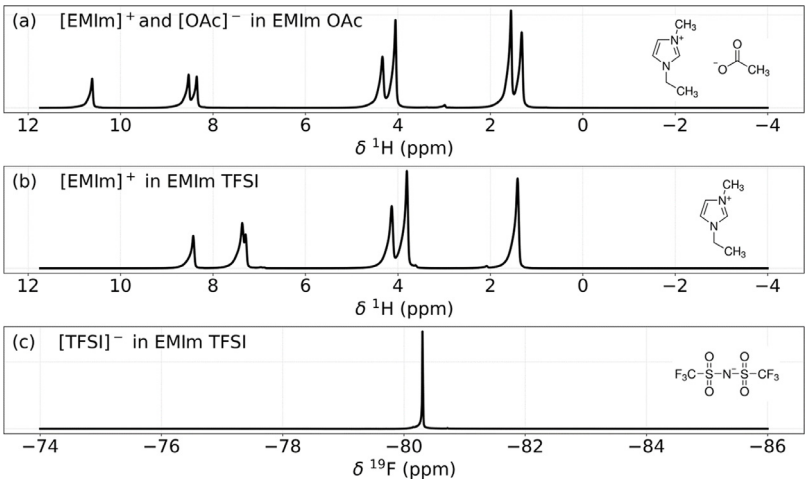

Fig. 4. ^{1}H NMR spectra of (a) $[EMIM]^{+}$ and $[OAc]^{-}$ in EMIm OAc, (b) $[EMIM]^{+}$ in EMIm TFSI, ^{19}F NMR spectra of (c) $[TFSI]^{+}$ in EMIm TFSI.

the knee frequency, the higher the diffusion rate [37]. Therefore, it is reasonable to state that the device containing EMIm TFSI has a higher electrolyte diffusion rate than the EMIm OAc-containing device.

The OCV was measured while the devices were being heated up in a 60 °C environment. Therefore, to correctly interpret the obtained results, it is essential to find out how the impedance characteristics change during the heating period, especially the influence of diffusion on capacitance and resistance. Fig. 3 (b_1) and (b_2) demonstrate EIS measurements with a single frequency of 500 mHz for a 3 h period while devices were being heated up. The frequency of 500 mHz is chosen because it is closest to the knee frequency (504 mHz) of EMIm TFSI containing device at RT. It is worth pointing out that the knee frequency of 504 mHz, as well as the other knee frequencies, has been selected visually and there might be some uncertainty regarding the values. Observing the EIS with 500 mHz (diffusion region in these systems) in both the devices will provide not only the information regarding changes of the impedance characteristics but will also minimize the uncertainty regarding the visual selection of the knee-values. It can be seen from Fig. 3 (b_1) and (b_2) that for both the devices capacitance increases and resistance decreases over time. The changes are abrupt in the beginning and reach equilibrium by 2000 s. The resistance decreases from 5.27 to 1.65 Ω cm^2 and 7.47 to 3.12 Ω cm^2 while capacitance increases from 22.83 to 77.31 F g^{-1} and 14.28 to 50.06 F g^{-1} for EMIm TFSI and EMIm OAc containing devices, respectively. These results validate that the high diffusion rate of EMIm TFSI positively contributes to the impedance performance.

However, at this point, it is worth mentioning that the diffusion rate revealed from EIS measurements is the mutual diffusion of both the ions present in the system. Therefore, even if the large difference of the voltage output between the two devices can be qualitatively correlated with the observed mutual diffusion rate difference, it is still necessary to investigate the distinct contribution of ions or the self-diffusion coefficient of individual ions of both the electrolytes to reach to a solid conclusion. In the next section, we discuss the self-diffusion coefficient of individual ions studied by NMR.

3.4. Self-diffusion coefficients of the ionic liquids

Fig. 4 shows the NMR spectra at RT of both neat EMIm OAc and EMIm TFSI ILs with the respective chemical groups present in the ILs. ^{1}H NMR spectra of $[EMIM]^{+}$ cation in both EMIM OAc and in EMIM TFSI, and $[OAc]^{-}$ anion in EMIM OAc are shown in Fig. 4 (a) and (b). ^{19}F NMR spectrum shown in Fig. 4 (c) exhibits a single peak associated with the $[TFSI]^{-}$ anion. The observed peaks are in agreement with previous studies [27,44,45].

Fig. 5 shows examples of the signal attenuation acquired in the pulsed-field gradient diffusion experiments. All signal attenuation plots follow a strictly mono-exponential decay pattern, which indicates an unimpeded diffusivity for the ions in the system at all temperatures investigated.

At a first glance, it is already noticeable that the signal decays are close to each other for $[EMIM]^{+}$ and $[OAc]^{-}$ in EMIm OAc electrolyte, see Fig. 5 (a), while more different slopes are observed for $[EMIM]^{+}$ and $[TFSI]^{-}$ in EMIm TFSI electrolyte, see Fig. 5 (b), at both RT and 60 °C. In other words, the diffusivity of cation and anion are more similar in EMIm OAc compared to the EMIm TFSI electrolyte.

Fig. 6 shows the calculated self-diffusion coefficients for all the ions in the entire temperature range. As both the ILs share the same cation $[EMIM]^{+}$, the observed difference should originate from the influence of the two anions $[OAc]^{-}$ and $[TFSI]^{-}$. The volume of the $[OAc]^{-}$ anion (39 Å^3 [35]) is significantly smaller than the $[TFSI]^{-}$ anion (100 Å^3 [46]), so it is natural to think that $[OAc]^{-}$ ions will display higher diffusivity than $[TFSI]^{-}$ ions. However, as can be seen, the opposite case is recorded: $[TFSI]^{-}$ ions have a higher self-diffusion coefficient than the $[OAc]^{-}$ throughout the temperature range, although the difference is not that large.

Most strikingly, the self-diffusion coefficients of $[EMIM]^{+}$ cations in the two systems are significantly different and seem to depend on their surrounding anions. As ILs are highly concentrated electrolytes, the movement of individual ions will largely depend on the coulombic interaction between the ions. Due to the smaller volume of $[OAc]^{-}$, the electric charge density would be much higher compared to the large $[TFSI]^{-}$. Therefore, $[EMIM]^{+}$ will have a stronger electric interaction with $[OAc]^{-}$ than with $[TFSI]^{-}$. It has been shown by molecular dynamics simulations that there is a stronger coordination between the cation and anion in EMIm OAc because $[OAc]^{-}$ ions form a strong hydrogen bond with $[EMIM]^{+}$ whereas no hydrogen bond is formed between $[TFSI]^{-}$ and $[EMIM]^{+}$ [45,47]. Therefore, the observed self-diffusion coefficient difference between the ions in the two ILs is mostly originating from the extent of ion pairing. $[OAc]^{-}$ does not move as a single ion, but rather in a pairing or cluster, therefore the diffusivity for both anion and cation is almost identical in EMIm OAc. On the other hand, $[TFSI]^{-}$ and $[EMIM]^{+}$ move more independently as single ionic species in EMIm TFSI electrolyte. It is worth pointing out

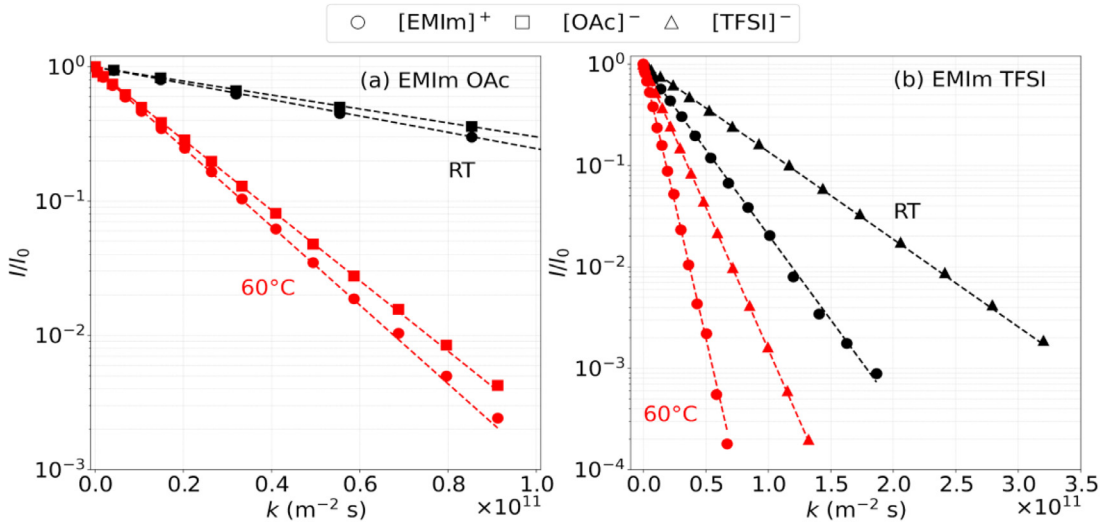

Fig. 5. NMR signal attenuation versus $k = (\gamma g \delta)^2(\Delta\text{-}\delta/3)$ for (a) $[EMIM]^+$, $[OAc]^-$ in EMIm OAc at RT and 60 °C respectively, (b) $[EMIM]^+$, $[TFSI]^-$ in EMIm TFSI at RT and 60 °C respectively.

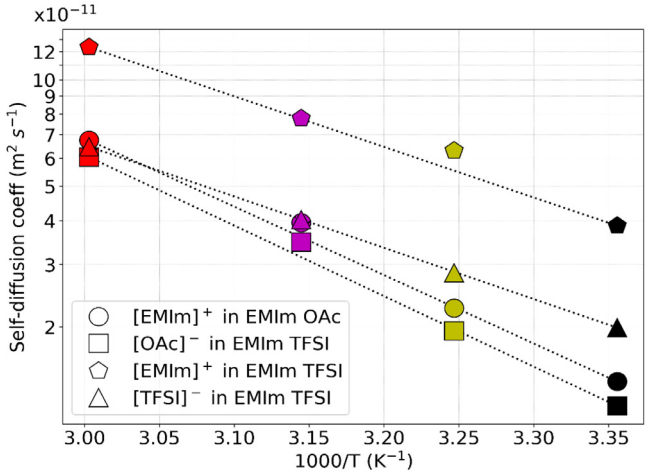

Fig. 6. Arrhenius plot of self-diffusion coefficients of individual ions in the studied temperature range.

that the self-diffusion coefficient of $[EMIm]^+$ is significantly higher than that of $[TFSI]^-$. In this case, the difference must be originating due to the smaller size of $[EMIm]^+$ cation (69 Å^3 [46], compared to 100 Å^3 for $[TFSI]^-$), which points out the relevance of ion size in the ionic mobility when the coulombic interaction is weak. The phenomenon has been previously observed in several studies with different anions [48,49], including the ions studied in this work.

The self-diffusion values in Fig. 6 are fitted with the Arrhenius equation as follows:

$$D = D_0 \exp(-E_a/RT) \quad (7)$$

where D is the self-diffusion coefficient, D_0 the pre-exponential factor (data fitting constant), E_a the activation energy, R the universal gas constant (8.31451 J mol^{-1} K^{-1}), and T the temperature in Kelvin.

The fitted data is linear enough to justify using the Arrhenius type equation. Accordingly, the activation energy is calculated from the slopes and listed in Table 3.

Here we report similar activation energy for the two ions in EMIm TFSI. The values are significantly lower than for the ions in EMIm OAc, which are also of similar value. Low and similar activation energy means that a lower and similar energy will be required

Table 3
Activation energy of individual ions self-diffusion calculated from Arrhenius plot.

Electrolyte	Ion	Activation energy (kJ mol^{-1})
EMIm	$[EMIM]^+$	26.0
TFSI	$[TFSI]^-$	26.5
EMIm	$[EMIm]^+$	37.6
OAc	$[OAc]^-$	38.8

for the self-diffusion of both the ions in EMIm TFSI compared to EMIm OAc. In addition, due to the large difference in the diffusivity of the ions in EMIm TFSI, there will be a larger asymmetry in the two interfaces causing a larger voltage output for EMIm TFSI electrolyte-containing device when exposed to heat compared to EMIm OAc containing device.

3.5. Potential of parallel life of supercapacitors

Traditional thermoelectric module made of metal/semiconductor/metal stack exposed in a temperature gradient generates a constant and continuous electrical output based on the well known electronic Seebeck effect, where the transport of charge carriers (electrons or holes) are bound by band structures. This electrical output can be delivered to an external load and during the process, there is no net transfer of material involved. On the other hand, an ionic thermoelectric system based on the thermogalvanic effect involves a net transfer of redox-active species between the hot and cold electrodes where the mass balance is satisfied with the ionic diffusion of oxidized and reduced species between the electrodes. Therefore, the voltage rise in a thermogalvanic cell occurs due to a combination of the thermodynamic shift in the chemical potential of redox species and the thermodiffusion of ionic species driven by the temperature gradient [4]. This working principle allows the thermocell to operate in a continuous mode like the conventional thermoelectrics and, the power density becomes the most relevant performance metric [5,50]. In an ionic thermoelectric system based on the ionic Seebeck effect, where the ions are not redox-active such as the system under current study, the thermodiffusive ions are the sole charge carriers and they can not pass through the external circuit no matter how they arrange on the electrode surface. Rather, the ions accumulate at the electrode/electrolyte interface and form

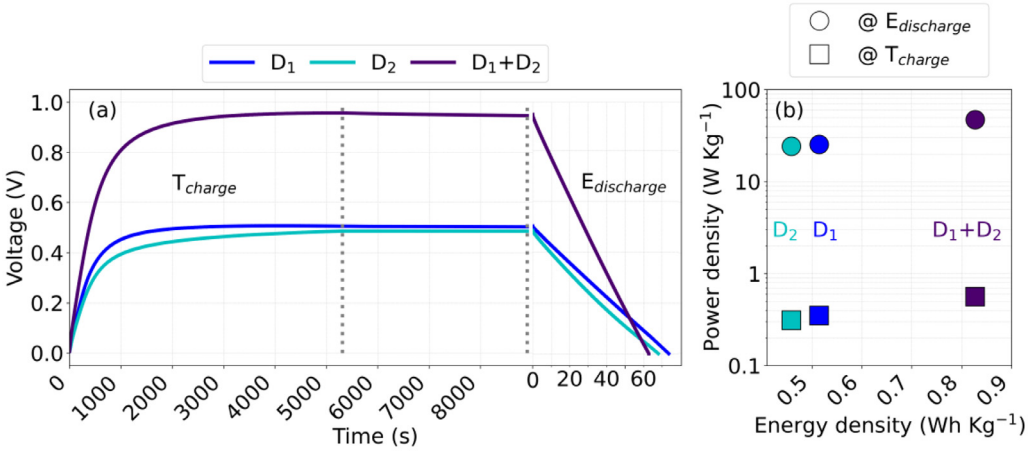

Fig. 7. (a) Voltage output of devices, D_1, D_2, and in series D_1+D_2, containing EMIm TFSI electrolyte and AC electrodes, (b) Ragone plot comparing energy density and power density in logarithmic scale from both thermal charging and electrical discharging.

an electric double layer (thermocapacitive effect [51]), inducing a transient current that decreases over time [5]. Therefore, the operation mode is not continuous but intermittent and both the energy density and power density are the relevant performance metric [50].

Fig. 7 demonstrates the thermal voltage output of two EMIm TFSI containing devices with AC electrodes, D_1 and D_2, stacked in series, which verifies the feasibility of larger voltage output. In this set of measurements, both the devices are individually exposed to 60 °C after one RT_{act}-cycle at 2.5 V, and accordingly, the stacked device containing D_1 and D_2 is exposed to heat after the RT_{act}-cycle at 5 V, see Fig. 7 (a).

The voltage recovery has been monitored throughout the heating and cooling period. A high voltage output of 502, 486, and 943 mV is achieved before the devices are electrically discharged with a constant current of 10 mA g^{-1} at RT. The capacitance is extracted from the discharge plot and calculated to be 59, 56, and 27 F g^{-1} for D_1, D_2, and D_1+D_2, respectively. The energy density of the devices is calculated to be 0.51, 0.46, and 0.83 W h kg^{-1}, which is plotted in the Ragone plot, Fig. 7 (b), along with the power density 25, 24, and 47 W kg^{-1} for D_1, D_2, and D_1+D_2, respectively, calculated from the electrical discharge curve.

Power density is also extracted from the thermal charging curve and calculated to be 349, 312, and 562 mW kg^{-1}. A significant difference between the power from thermal charging and electrical discharging is reasonable due to the large time difference in thermal charging and electrical discharging. In general, thermoelectric effects are useful for low power energy harvesting and therefore suitable for slowly charging an electrochemical storage device, SC, or batteries followed by a rapid discharge as a high power pulse [4,5]. Generally, power demands for the internet of things (IoT) sensors range from μW to mW with a relatively high operating voltage of 1–5 V [4]. Therefore, the observed increased voltage, energy, and power density of the stacked device point out the possibility of connecting more devices in series or parallel depending on the application requirements.

In practice, the ionic thermoelectric effect in this system works as an internal electric generator that charges the electric double layer of the SCs with large capacitance. The following equivalent circuit (Fig. 8) can represent the system under study.

The operation can be carried out in two ways. (I) Direct thermal charging, whereupon exposing to high-temperature environment SC develops a spontaneous open circuit thermal voltage which can effectively be utilized through an external load either at the high-temperature environment or at RT enabling energy harvesting from

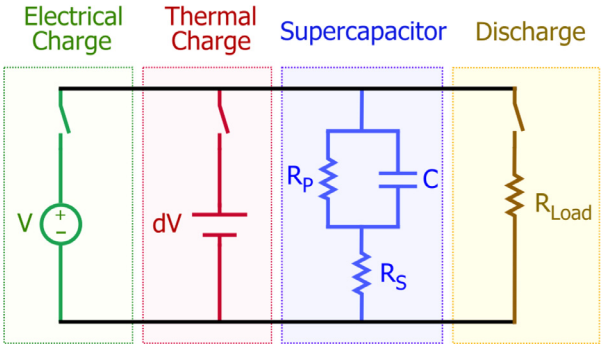

Fig. 8. Equivalent circuit of thermal charging and discharging process of the ionic thermoelectric system.

heat source followed by energy storage and utilization without any strict requirement of heat source. (II) Voltage recovery with heat after an electrical charge/discharge cycle, whereupon applying heat to the device after a typical electrical operation the unused energy can be recovered faster due to the thermally induced enhancement in the kinetics of the process involved in charge storage and could be also utilized at the high-temperature environment or RT. From this perspective, this ionic thermoelectric system integrates two different functions, energy harvesting and energy storage in a single multitasking device that opens up the possibility to give a parallel life to SCs.

3.6. Towards the optimum performance of thermoionic capacitor

Low specific heat capacity, low thermal conductivity, and high ionic/electronic conductivity are the vital prerequisites for typical thermoelectrics and ionic thermoelectric system that works within a fixed temperature gradient [10]. In this regard, ILs are particularly preferable because they can ensure the long-term maintenance of temperature gradient between the electrodes due to their very low thermal conductivity, typically around 0.2 W m^{-1} K^{-1} compared to water (aqueous electrolyte) that is 0.62 W m^{-1} K^{-1}, although aqueous electrolytes possess higher ionic conductivity [52]. However, in the current system, where the devices are working in a homogeneously changing temperature, heat capacity could be a more relevant defining factor to the device performance. The reported specific heat capacity is found to be 0.836 J g^{-1} K^{-1} for EMIm TFSI whereas 1.868 J g^{-1} K^{-1} for EMIm OAc [40]. This indicates that lower energy would be needed in the heating process [53] for

EMIm TFSI containing devices to achieve a particular thermovoltage compared to EMIm OAc-containing device.

In the absence of a chemical redox reaction, the thermovolatge is mainly originating from the extent of rearrangement and migrations of ions in the interface. It is worth emphasizing that thermally driven migration of ions in ionic conductors (electrolytes) is a natural phenomenon but for them to exhibit noticeable thermoelectric properties there has to be a difference in the thermal migration rate between the anions and cations. For example, both the studied ILs exhibit a similarly increased ionic conductivity, and reduced viscosity with increasing temperature along with the improved impedance characteristics of the devices such as ESR, diffusion rate, and capacitance. Yet EMIm TFSI containing device demonstrates a significantly higher thermovoltage and that is mainly due to a larger difference in the migration ability between the cations and anions. The difference in the migration ability could be further enlarged by controlling the surface of carbon electrodes with either more positively or negatively charged functional groups that will favor either anion or cation adsorption/desorption.

4. Conclusions

A systematic investigation is carried out to explore the thermal charging of SCs containing two different ILs, EMIm TFSI, and EMIm OAc, with activated carbon electrodes, as an ionic thermoelectric system working in the low-grade heat regime (60 °C).

The study reveals that a significant voltage output can be achieved without any fixed temperature gradient but rather with a homogeneous change in temperature, due to asymmetry in the two electrical double layer interfaces. The EMIm TFSI containing device exhibits a greater performance regarding voltage output in different conditioning compared to the EMIm OAc containing device. The asymmetry arises due to a significant difference in the self-diffusion coefficient between $[EMIM]^+$ and $[TFSI]^-$ ions in EMIM TFSI electrolyte as compared to $[EMIM]^+$ and $[OAc]^-$ in EMIM OAc electrolyte. The asymmetry in the interfaces does not negatively influence the regular electrical performance. Moreover, the unused energy in the typical electrical charge/discharge cycle, due to a large mismatch between the fast kinetics of electrons in AC electrodes and slower kinetics of electrolyte ions, is recovered with high-temperature exposure. When two EMIm TFSI containing devices are stacked in series, a large voltage output of 943 mV can be achieved with an energy density of 0.83 W h kg^{-1} and a power density of 47 W kg^{-1}, which is competitive to any other thermoionic system. The devices remain charged even if they are removed from the heat and can therefore be discharged while supplying a current to an external load.

The knowledge gained from this study opens up the possibility to take advantage of the inherent asymmetry between two interfaces that could originate from various ILs. Moreover, a working mechanism without a fixed temperature gradient adds an enormous design advantage as establishing and maintaining a fixed temperature gradient in a low-grade heat regime is not trivial.

Declaration of Competing Interest

The authors declare that they have no known competing financial interests or personal relationships that could have appeared to influence the work reported in this paper.

Credit authorship contribution statement

Mazharul Haque: Conceptualization, Methodology, Investigation, Visualization, Data curation, Writing – original draft, Writing – review & editing, Formal analysis. **Iqbaal Abdurrokhman:** Methodology, Investigation, Writing – review & editing, Resources. **Alexander Idström:** Methodology, Investigation, Writing – review & editing, Formal analysis, Resources. **Qi Li:** Conceptualization, Methodology, Writing – review & editing, Resources. **Azega Rajaras:** Data curation, Investigation. **Anna Martinelli:** Writing – review & editing, Formal analysis, Resources. **Lars Evenäs:** Writing – review & editing, Formal analysis, Methodology, Resources. **Per Lundgren:** Writing – review & editing, Supervision, Project administration. **Peter Enoksson:** Supervision, Project administration, Funding acquisition, Writing – review & editing.

Acknowledgments

The authors gratefully acknowledge European Union's Horizon 2020 research and innovation program under grant agreement no 101006963 (GreEnergy), Vinnova UDI project Miniaturized self-powered industrial sensor systems using energy harvesting technologies-Energy Supply Toolkit (2017–03725), Architectures for High-Power Radars (2017–04869), Chalmers Area of Advance Material Science, Chalmers Area of Advance project Microelectronic Energy Storage systems for Integration Alongside Harvesters (MESSIAH), and The Wallenberg Wood Science Center (WWSC) funded by Knut and Alice Wallenberg Foundation for the support of this work. The NMR measurements were carried out at the Swedish NMR Center, Gothenburg, Sweden.

Supplementary materials

Supplementary material associated with this article can be found, in the online version, at doi:10.1016/j.electacta.2021.139640.

References

[1] C. Forman, I.K. Muritala, R. Pardemann, B. Meyer, Renew. Sustain. Energy Rev 57 (2016) 1568–1579.
[2] X. Zhang, M. He, Y. Zhang, Renew. Sustain. Energy Rev 16 (2012) 5309–5318.
[3] G.J. Snyder, E.S. Toberer, in: Complex Thermoelectric Materials, Nature Publishing Group, 2011, pp. 101–110.
[4] W. Liu, X. Qian, C.G. Han, Q. Li, G. Chen, Appl. Phys. Lett 118 (2021) 020501.
[5] H. Wang, D. Zhao, Z.U. Khan, S. Puzinas, M.P. Jonsson, M. Berggren, X. Crispin, Adv. Electron. Mater. 3 (2017) 1700013.
[6] D. Zhao, A. Würger, X. Crispin, J. Energy Chem. 61 (2021) 88–103.
[7] A. Al-zubaidi, X. Ji, J. Yu, Sustain. Energy Rev. 1 (2017) 1457–1474.
[8] H. Lim, Y. Shi, Y. Qiao, Appl. Phys. A 122 (2016) 443.
[9] J.J. Wang, S.P. Feng, Y. Yang, N.Y. Hau, M. Munro, E. Ferreira-Yang, G. Chen, Nano Lett. 15 (2015) 5784–5790.
[10] D. Zhao, H. Wang, Z.U. Khan, J. Chen, R. Gabrielsson, M.P. Jonsson, M. Berggren, X. Crispin, Energy Environ. Sci. 9 (2016) 1450–1457.
[11] C. Subramaniam, T. Pradeep, J. Chakrabarti, J. Phys. Chem. C 111 (2007) 19103–19110.
[12] B. Xu, Y. Qiao, T. Park, M. Tak, Q. Zhou, X. Chen, Energy Environ. Sci. 4 (2011) 3632–3639.
[13] B. Xu, B. Wang, T. Park, Y. Qiao, Q. Zhou, X. Chen, J. Chem. Phys. 136 (2012) 184701.
[14] D. Lee, Langmuir 23 (2007) 6011–6018.
[15] J.W. Graydon, M. Panjehshahi, D.W. Kirk, J. Power Sources 245 (2014) 822–829.
[16] C. Zhong, Y. Deng, W. Hu, J. Qiao, L. Zhang, J. Zhang, Chem. Soc. Rev. 44 (2015) 7484–7539.
[17] E. Laux, S. Uhl, T. Journot, J. Brossard, L. Jeandupeux, H. Keppner, J. Electron. Mater. 45 (2016) 3383–3389.
[18] M. Armand, F. Endres, D.R. MacFarlane, H. Ohno, B. Scrosati, Nat. Mater. 8 (2009) 621–629.
[19] V. Lesch, S. Jeremias, A. Moretti, S. Passerini, A. Heuer, O. Borodin, J. Phys. Chem. B 118 (2014) 7367–7375.
[20] M. Jeyapandian, S. Lavina, S. Thayumanasundaram, H. Ohno, E. Negro, V. Di Noto, J. Power Sources 195 (2010) 341–353.
[21] M. Haque, Q. Li, A.D. Smith, V. Kuzmenko, E. Köhler, P. Lundgren, P. Enoksson, Electrochim. Acta 263 (2018) 249–260.
[22] G. Pagot, F. Bertasi, K. Vezzù, G. Nawn, G. Pace, A. Nale, V. Di Noto, Solid State Ion. 320 (2018) 177–185.
[23] F. Bertasi, G. Pagot, K. Vezzu, A. Nale, G. Pace, Y.H. Bang, G. Crivellaro, E. Negro, V. Di Noto, Electrochim. Acta 307 (2019) 51–63.
[24] M. Holz, H. Weingartner, J. Magn. Reson. 92 (1991) (1969) 115–125.
[25] E. Stejskal, J. Chem. Phys. 43 (1965) 3597–3603.
[26] D.W. Marquardt, J. Soc. Ind. Appl. Math. 11 (1963) 431–441.
[27] A.C. Forse, J.M. Griffin, C.I. Merlet, P.M. Bayley, H. Wang, P. Simon, C.P. Grey, J. Am. Chem. Soc. 137 (2015) 7231–7242.

[28] S. Fletcher, I. Kirkpatrick, R. Dring, R. Puttock, R. Thring, S. Howroyd, J. Power Sources 345 (2017) 247–253.
[29] R. De Levie, Electrochim. Acta 8 (1963) 751–780.
[30] S. Fletcher, V.J. Black, I. Kirkpatrick, J Solid State Electrochem. 18 (2014) 1377–1387.
[31] T.J. Abraham, D.R. MacFarlane, J.M. Pringle, Energy Environ. Sci. 6 (2013) 2639–2645.
[32] H. Jia, X. Tao, Y. Wang, Adv. Electron. Mater. 2 (2016) 1600136.
[33] M. Haque, Q. Li, A.D. Smith, V. Kuzmenko, P. Rudquist, P. Lundgren, P. Enoksson, J. Power Sources 453 (2020) 227897.
[34] M. Haque, Q. Li, C. Rigato, A. Rajaras, A.D. Smith, P. Lundgren, P. Enoksson, J. Power Sources 485 (2021) 229328.
[35] L. Guan, L. Yu, G.Z. Chen, Electrochim. Acta 206 (2016) 464–478.
[36] F. Béguin, V. Presser, A. Balducci, E. Frackowiak, Adv. Mater. 26 (2014) 2219–2251.
[37] K.L. Van Aken, J.K. McDonough, S. Li, G. Feng, S.M. Chathoth, E. Mamontov, P.F. Fulvio, P.T. Cummings, S. Dai, Y. Gogotsi, J. Condens, Matter Phys. 26 (2014) 284104.
[38] H. Tokuda, K. Hayamizu, K. Ishii, M.A.B.H. Susan, M. Watanabe, J. Phys. Chem. B 109 (2005) 6103–6110.
[39] O. Okoturo, T. VanderNoot, J. Electroanal. Chem. 568 (2004) 167–181.
[40] E. Fabre, S.S. Murshed, J. Mater. Chem. A (2021) 15861.
[41] A. Nazet, S. Sokolov, T. Sonnleitner, T. Makino, M. Kanakubo, R. Buchner, J. Chem. Eng. 60 (2015) 2400–2411.
[42] G. Paasch, K. Micka, P. Gersdorf, Electrochim. Acta 38 (1993) 2653–2662.
[43] P. Yu, B.N. Popov, J.A. Ritter, R.E. White, J. Electrochem. Soc. 146 (1999) 8.
[44] V.V. Matveev, D.A. Markelov, A.V. Ievlev, E.A. Brui, K.V. Tyutyukin, E. Lähderanta, Magn. Reson. Chem. 56 (2018) 140–143.
[45] C. D'Agostino, M.D. Mantle, C.L. Mullan, C. Hardacre, L.F. Gladden, ChemPhysChem 19 (2018) 1081–1088.
[46] A.W. King, A. Parviainen, P. Karhunen, J. Matikainen, L.K. Hauru, H. Sixta, I. Kilpeläinen, RSC Adv. 2 (2012) 8020–8026.
[47] T.G. Youngs, J.D. Holbrey, C.L. Mullan, S.E. Norman, M.C. Lagunas, C. D'Agostino, M.D. Mantle, L.F. Gladden, D.T. Bowron, C. Hardacre, Chem. Sci. 2 (2011) 1594–1605.
[48] K. Hayamizu, Y. Aihara, H. Nakagawa, T. Nukuda, W.S. Price, J. Phys. Chem. B 108 (2004) 19527–19532.
[49] R.C. Remsing, G. Hernandez, R.P. Swatloski, W.W. Massefski, R.D. Rogers, G. Moyna, J. Phys. Chem. B 112 (2008) 11071–11078.
[50] X. Shi, J. He, Science 371 (2021) 343–344.
[51] A. Härtel, M. Janssen, D. Weingarth, V. Presser, R. van Roij, Energy Environ. Sci. 8 (2015) 2396–2401.
[52] X. Wu, N. Gao, H. Jia, Y. Wang, Chem. Asian J. 16 (2021) 129–141.
[53] Y. Yang, S.W. Lee, H. Ghasemi, J. Loomis, X. Li, D. Kraemer, G. Zheng, Y. Cui, G. Chen, PNAS 111 (2014) 17011–17016.